Optimal design of the annular groove phase mask central region

Konig, Lorenzo; Absil, Olivier; Lobet, Michael; Delacroix, Christian; Karlsson, Mikael; De Xivry, Gilles Orban; Loicq, Jerome

Published in:
Optics Express

DOI:
10.1364/OE.461047

Publication date:
2022

Document Version
Publisher's PDF, also known as Version of record

Research Article | Vol. 30, No. 15 / 18 Jul 2022 / Optics Express 27048
Optics EXPRESS

Optimal design of the annular groove phase mask central region

LORENZO KÖNIG,[1,*] OLIVIER ABSIL,[1] MICHAËL LOBET,[2] CHRISTIAN DELACROIX,[1] MIKAEL KARLSSON,[3] GILLES ORBAN DE XIVRY,[1] AND JÉRÔME LOICQ[4,5]

[1]*STAR Institute, Université de Liège, Allée du Six Août 19C, 4000 Liège, Belgium*
[2]*Laboratoire de Physique du Solide and Namur Institute for complex systems (naXys), University of Namur, Rue de Bruxelles 61, 5000 Namur, Belgium*
[3]*Department of Materials Science and Engineering, Uppsala University, Box 35, 751 03 Uppsala, Sweden*
[4]*Faculty of Aerospace Engineering, Delft University of Technology, 2629 HS Delft, The Netherlands*
[5]*Centre Spatial de Liège, Université de Liège, Avenue du Pré-Aily, 4031 Angleur, Belgium*
[*]*lorenzo.konig@uliege.be*

Abstract: Vortex phase masks have been shown to be an efficient means to reduce the blinding stellar light in high-contrast imaging instruments. Once placed at the focal plane of the telescope, the helical phase ramp of a vortex phase mask diffracts the light of a bright on-axis source outside the re-imaged telescope pupil, while transmitting the light of a faint off-axis companion nearly unaffected. The Annular Groove Phase Mask (AGPM) is a broadband metasurface implementation of a vector vortex phase mask using the artificial birefringence of a circular subwavelength grating etched onto a diamond substrate. To date, the AGPM design has been optimized using rigorous coupled-wave analysis (RCWA), which is a valid tool to simulate periodic straight gratings. However, we have now reached a performance level where the curvature of the grating lines at the center becomes a limiting factor. Here, we use a finite-difference time-domain (FDTD) method to correctly describe the AGPM performance, including the effect of the curved grating close to its center. We confirm the validity of this simulation framework by comparing its predictions with experimental results obtained on our infrared coronagraphic test bench, and we show that RCWA fails at reproducing correctly the central AGPM performance, confirming the need for a full 3d simulation tool such as FDTD. Finally, we use FDTD to optimize the grating parameters at the AGPM center, and conclude with a new optimal design.

1. Introduction

In observational astronomy, high-contrast imaging of exoplanets faces two main challenges. On the one hand, it needs the angular resolution of very large telescopes to distinguish between the diffraction pattern of a star and its planetary companion. On the other hand, the huge contrast between the bright host star and its faint companion, ranging from 10^3 for gas giants orbiting young stars to 10^{10} for Earth-like planets around solar-type stars, needs to be addressed. An efficient adaptive optics system and a performing coronagraph can tackle these issues. In the case of the METIS instrument to be installed at the Extremely Large Telescope, the required raw contrast is 2×10^{-3} across a spectral bandwidth of up to 50% [1]. A vortex coronagraph can fulfil these requirements by reducing the contrast by several orders of magnitude over a considerable spectral bandwidth [2].

The annular groove phase mask (AGPM) is an implementation of a vector vortex phase mask that was proposed in 2005 to provide the necessary contrast requirements to achieve this performance over a broad wavelength range [3]. Since then, several AGPMs have been successfully manufactured and installed on some of the world's most advanced optical telescopes [4–7]. The AGPM uses the artificial birefringence of a subwavelength grating etched onto a

#461047 https://doi.org/10.1364/OE.461047
Journal © 2022 Received 19 Apr 2022; revised 1 Jun 2022; accepted 10 Jun 2022; published 12 Jul 2022

Optics EXPRESS

diamond substrate to produce the characteristic helical phase ramp of an optical vortex at its center [8]. Historically, the artificial birefringence of subwavelength gratings was first proposed in the field of stellar coronagraphy to enable a broadband implementation of the four quadrant phase mask [9,10]. The grating parameters are tuned to act as an achromatic half wave plate, introducing a π phase shift between orthogonal polarizations. This allows to imprint a geometric phase purely determined by the orientation of the grating. The orientation of the grating lines is changed around the optical axis so as to provide the desired (even) topological charge, which describes the number of intertwined helices making the wavefront. Figure 1 shows the theoretical pattern of the subwavelength grating vortex phase mask for topological charge two. The relevant design parameters of the grating are the period Λ, the filling factor F, and the grating height h. The slope α of the grating side walls is fixed by the manufacturing process. Manufacturing of the AGPM is achieved using nanoimprint lithography and a multi-step plasma etching process, as described in [11]. Other implementations of vortex phase masks exist, such as the liquid crystal polymer optical vector vortex coronagraph using the birefringence of liquid crystal polymers to generate the phase ramp [12].

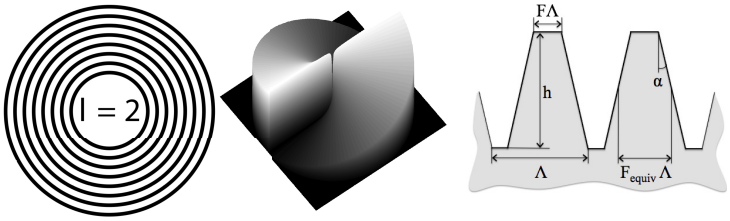

Fig. 1. The subwavelength grating vortex coronagraph for topological charge $l = 2$. (a) Theoretical grating pattern, (b) helical phase ramp, and (c) grating profile illustrating the grating parameters.

AGPMs can be understood as a specific implementation of an all-dielectric metasurface. Metasurfaces are thin structures operating in the subwavelength domain with the size of their constituent unit cells smaller than the wavelength of illumination [13]. The shape, orientation and material of the basic building blocks of the unit cell affect the incoming wave propagation. Applications of metasurfaces are widely spread, ranging e.g. from communication [14] to achromatic flat optical devices [15], including applications in astronomical instrumentation [16]. Several applications of all-dielectric vortex beam converters have already been reported in the literature [17–19]. Here, the considered subwavelength gratings are a type of metasurface with increased symmetry. One of their key characteristics compared to standard metasurfaces is that they provide high performance across large spectral bandwidths.

So far, the AGPM performance has been studied with the rigorous coupled wave analysis (RCWA) method [20], which is a suitable tool to explore periodic structures. Periodic and consequently infinite straight gratings are optimized using this RCWA simulation strategy [21]. Using this approach, several AGPMs have been successfully designed and manufactured providing excellent results [11]. However, we have now reached a performance level where the validity of these simulation tools is questioned by the curvature of the grating lines, which is most prominent near the center of the mask (see Section 3). A full 3d simulation tool is required to describe correctly the central region and to estimate its impact on the performance of the full AGPM. Such a 3d simulation tool is also interesting for designing new all-dielectric metasurface solutions for vortex phase masks of charge-2 (AGPM-like) or of higher topological charge, which will be needed for future Extremely Large Telescopes [22]. The finite-difference time-domain (FDTD) method provides an adequate framework to study the effect of curved grating lines by simulating

Optics EXPRESS

only a finite patch of the AGPM around its center. Despite being computationally more expensive than RCWA, FDTD makes it possible to define the limits of RCWA in terms of curvature and periodicity. FDTD is therefore suited to explore new designs for the center of the AGPM as well as to simulate metasurfaces of more complex shapes.

In this paper, we use the open-source FDTD code MEEP [23] to simulate the AGPM. In Section 2, we first use MEEP to confirm the results of our RCWA simulations considering a finite patch of parallel grating lines. We then use MEEP to simulate the central part of the AGPM, and show that the RCWA results clearly deviate from the FDTD results (Section 3). In Section 4, we experimentally confirm the predicted performance decrease due to the AGPM center. Finally, we investigate in Section 5 the influence of the central pattern on the performance of the AGPM center and come up with a new, optimal design. Throughout this paper, we consider an AGPM for application in the *L*-band atmospheric window ($2.9 - 4.1\,\mu$m). Because of the scale invariance of the problem, the results can be appropriately scaled to other wavelength ranges, such as visible or telecommunication wavelengths.

2. Benchmarking FDTD against RCWA simulations

2.1. Performance metric

Two equivalent metrics are used in the literature to assess the performance of the AGPM: the null depth and its inverse, the rejection ratio. Throughout this paper we will use the null depth, which represents the fractional leakage of the stellar light through the coronagraph [3]. For clarity, we will distinguish between the null depth, which refers to the global performance of an AGPM, and the intrinsic leakage of the grating, which refers to the fractional amount of light leaking through a periodic infinite straight grating calculated with RCWA. Despite the broadband character of the AGPM, the grating does not behave as an exact half wave plate over the full spectral bandwidth, which leads to a fraction of the stellar light leaking through the coronagraph (typically 0.1 %, [24]). In theory, the null depth can be predicted based on the phase and intensity mismatch between the TE and TM modes of the grating (i.e., the linear polarizations parallel and orthogonal to the grating lines, respectively), which are both simulated independently using RCWA. Within FDTD simulations, we instead directly measure the leakage intensity after the grating at the focal plane, using an incident circularly polarized plane wave, which is a good description of the center of the Airy disk at the focal plane. Our simulations propagate the beam only just before and after the grating, which corresponds to the inset in Fig. 2, where the handedness of the input polarization is flipped by the half wave plate character of the AGPM. The outgoing circular polarizations represent respectively the leakage (with same handedness as the incident wave) and the converted vortex beam (with opposite handedness), which are both normalised by the total transmitted flux.

2.2. Simulation tools

We use the open source FDTD code MEEP [23] to simulate a finite patch of the AGPM. While it would in principle be possible to simulate the whole AGPM using FDTD, there is no need to do so. In fact, the grating far from the center is sufficiently parallel and can be described properly with RCWA. In the following, we will therefore first validate our results obtained with RCWA using a finite patch of parallel grating lines (i.e., the outer part of the AGPM), and then focus solely on the central part of the AGPM with FDTD simulations.

The null depth and the phase ramp imprinted on the converted wave are monitored after the grating, inside the diamond substrate. We use perfectly matched layers (PMLs) to suppress reflections at the cell boundaries [25]. PMLs consist of an artificial absorbing boundary layer with matched impedance suppressing reflection artefacts at the cell boundaries. Not using PMLs would mean simulating an isolated patch instead of a part of a larger continuous structure.

Optics EXPRESS

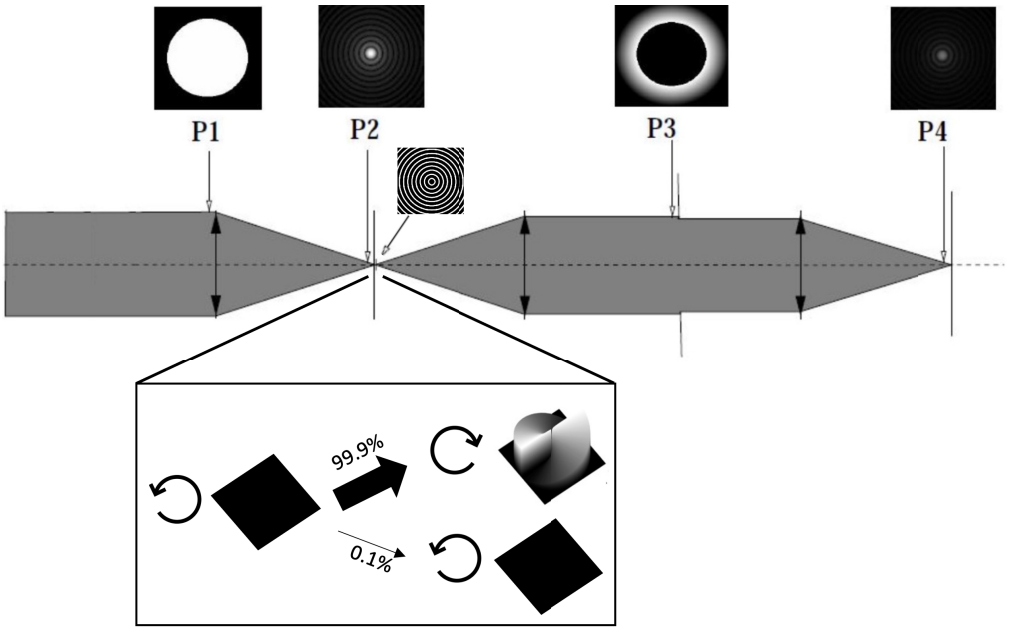

Fig. 2. Setup of the Vortex Coronagraph. (P1) Entrance pupil, (P2) focal plane with the AGPM, (P3) Lyot plane, and (P4) image plane. The incoming circular polarization is flipped by the AGPM and acquires the characteristic helical phase ramp. Due to the broadband character of the AGPM, a small fraction of the incoming light (in the order of 0.1 %) is transmitted unaffected, resulting in the leakage PSF.

The PMLs have to be sufficiently thick to reduce the reflection artefacts as much as possible. In our case, most of the simulation cell is occupied by PMLs (a physical simulation cell of $36\,\mu m \times 36\,\mu m \times 11\,\mu m$ surrounded by $12\,\mu m$ PMLs on all sides means 89 % of the total volume is used up by PMLs). Another critical requirement for MEEP is to reach a high simulation accuracy, because the null depth of an AGPM is typically of the order of 10^{-3}. This increases the computational load drastically, since in MEEP doubling the resolution increases the memory consumption by a factor 2^3, and the computation time by a factor 2^4. We therefore choose to make a compromise between accuracy and computational resources available, ensuring that the necessary accuracy of the results is reached.

2.3. *Finite straight grating lines patch simulation with FDTD*

We start by validating our MEEP simulation framework against RCWA simulations in a simple case of a straight grating, for which RCWA is known to be valid, by considering a finite patch of straight grating lines in MEEP with the grating geometry displayed in Fig. 1(c). Figure 3(a) and 3(b) show the grating design for our chosen patch size of $33\,\Lambda \times 33\,\Lambda$, and the leakage distribution after the grating for an illuminating wavelength $\lambda = 3.5\,\mu m$. Because the AGPM grating line orientation changes with azimuth, we need to ensure that all grating orientations are sufficiently well described with MEEP. Here, we use a grating oriented at 45° from the cartesian cell axes because, as illustrated below, the convergence of the null depth in MEEP simulations is slower for diagonal grating lines than for grating lines parallel to the cartesian axes. Due to the non-zero side wall angle illustrated in Fig. 1(c), it must be noted that the filling factor F varies along the optical axis (z-axis). In Fig. 3(a), and in all following figures, we choose to show the filling factor at half grating height, because it is more representative of the effective material

Optics EXPRESS

distribution inside the grating than the nominal filling factor F at the top of the grating. The simulations still take into account the trapezoidal profile of the grating.

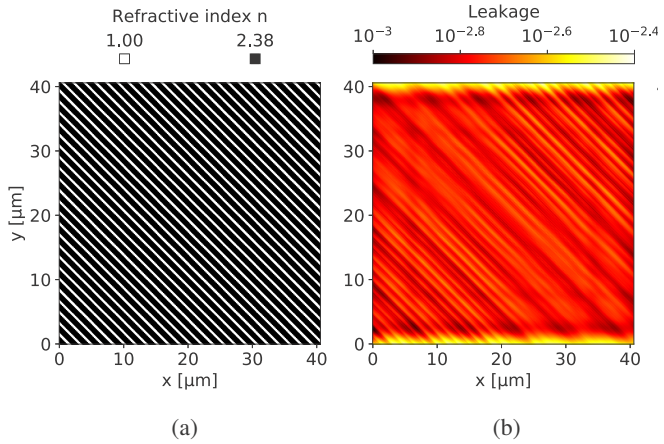

Fig. 3. (a) Grating design and (b) leakage distribution simulated with FDTD for a finite patch of straight grating lines at $\lambda = 3.5\,\mu$m. The leakage is normalized by the total transmitted flux. Optimal grating parameters for the L-band ($2.9 - 4.1\,\mu$m) are used: $\Lambda = 1.21\,\mu$m, $F = 0.5373$, $h = 5.5343\,\mu$m, $\alpha = 2.45°$. The grating is etched into a diamond substrate with refractive index $n \simeq 2.38$ in this wavelength range.

Since we use the same grating parameters as for the RCWA simulation, we expect similar results for the leakage, provided that a patch of $33\,\Lambda \times 33\,\Lambda$ is sufficiently representative of the infinite straight grating assumed by RCWA. Figure 4 shows the spectral leakage measured with MEEP, compared to the RCWA results for an optimally designed grating (optimal in the sense of RCWA). We show the results for both diagonal (Fig. 4(a)) and horizontal (Fig. 4(b)) grating lines, and for different values of the MEEP resolution, ranging from 14pxl/µm to 23pxl/µm. A monochromatic MEEP simulation of this size at a resolution of 23pxl/µm needs 2700 CPUh using 170 GB RAM, while the equivalent RCWA simulation only takes 40 seconds on a recent laptop, which illustrates the high computational load of MEEP. For diagonal grating lines, the results of the MEEP simulations differ by an absolute leakage of the order of 10^{-3} from the RCWA results for a resolution higher than 20pxl/µm. This discrepancy is acceptable, considering that we are simulating a finite patch instead of an infinite structure, and considering the simulation artefacts visible in Fig. 3(b), which could account for deviations in the results. Also, we will use MEEP mainly to simulate the AGPM center, where the leakage values are higher than for the off-axis patch presented in this section: typically the leakage at the center is in the order of 10^{-1}, which is large compared to our simulation accuracy of 10^{-3} for straight grating lines. For horizontal lines, the results converge at 17pxl/µm, while for diagonal lines the results are not converged even at 23pxl/µm, which is the limit of what we can simulate in terms of computational resources. To keep computational time reasonable, we choose a resolution of 20pxl/µm, which is sufficient to reach the needed accuracy. The difference in the matching accuracy for both grating orientations is due to the sub-pixel averaging used in MEEP to define the permittivity function. This feature is crucial to define a material distribution representative of the actual geometry. For horizontal grating lines parallel to the cartesian cell axes, the sub-pixel averaging is done in one dimension (normal to the grating lines) while for diagonal lines the averaging has to be done in two dimensions. Simulations with other grating parameters yield similar results. Despite the non-negligible discrepancy of the results for diagonal grating lines, we conclude that MEEP at a

Optics EXPRESS

resolution of 20pxl/µm is an appropriate tool to simulate a finite patch of the AGPM, and well suited to simulate the center.

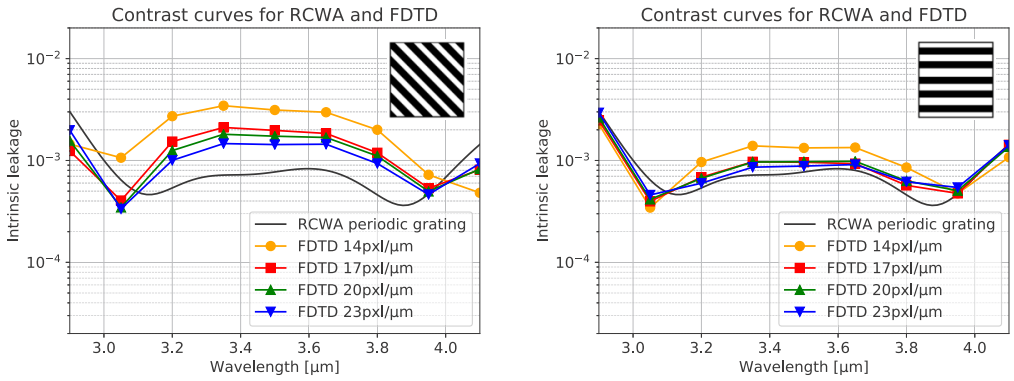

Fig. 4. Intrinsic leakage for a 33 Λ × 33 Λ patch of straight grating lines for a given set of grating parameters calculated with RCWA (black) and FDTD (colored). (a) Diagonal grating lines, and (b) horizontal grating lines. The low number of simulation points is due to the high computational cost of FDTD. Optimal grating parameters for the *L*-band (2.9 − 4.1 µm) are used: Λ = 1.21 µm, $F = 0.5373$, $h = 5.5343$ µm, $\alpha = 2.45°$.

3. AGPM center simulations

After confirming the validity of MEEP for straight grating simulations, we consider the center of the AGPM, where the conditions needed for RCWA are not satisfied anymore. We use a finite patch of the AGPM center including the first 15 grating lines, with a size of 30 Λ × 30 Λ. This region corresponds to a patch of radius $0.2\lambda/D$ for an AGPM illuminated at f/47 with $\lambda = 3.5$ µm. Figure 5 shows the design, the resulting leakage, and the phase ramp for an AGPM with optimal design parameters (in the sense of RCWA) at an illuminating wavelength $\lambda = 3.5$ µm. Figure 5(b) clearly shows the central region of increased leakage, which is higher than expected by RCWA. This can be used to define the limit of validity of RCWA in terms of grating line curvature, in the case of the AGPM. The size of the increased leakage region actually depends on the illuminating wavelength and on the details of the central grating geometry, notably the size of the central pillar or hole (see Appendix A for more details). For a central pillar with a diameter similar to the grating period, as used here, the central leakage is mostly localized in a circle with radius 5 Λ. This result means that we can rely on RCWA to describe the AGPM beyond 5 Λ from the center, and that we only need to simulate the first five grating lines with FDTD. However because the central leakage region depends on the wavelength, and on the grating design to some level, we choose to use a larger simulation region of radius 15 Λ when optimizing the central design, to ensure that all the central leakage is included (Section 5).

For a realistic estimate of the null depth of an AGPM, it is important to consider the contribution of the central leakage term to the null depth of the full mask. This can be done by calculating the central leakage with FDTD, and by assuming that RCWA describes well the AGPM far from the center. In practice, the AGPM is usually illuminated by an Airy pattern, assuming a circular telescope aperture and an efficient adaptive optics correction. The central region of the AGPM, where the curvature of the grating is high, generally covers a small fraction of the central Airy disk. By dividing the AGPM into a region of approximately periodic lines, and another region close to the center with curved lines, we can calculate the amount of flux incident on both regions, depending on the *f*-number (i.e., the ratio of the focal length to the pupil diameter). We then

Optics EXPRESS

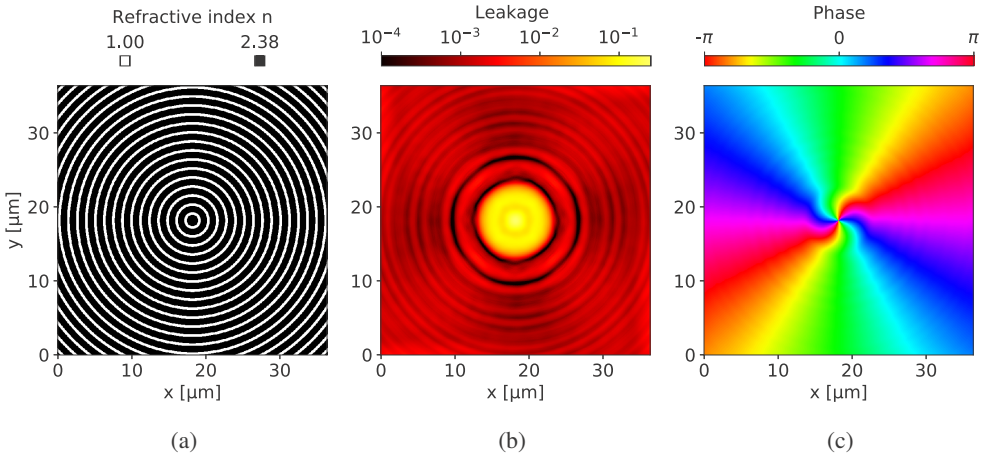

Fig. 5. (a) Design, (b) leakage and (c) phase ramp simulated with FDTD at $\lambda = 3.5\,\mu\text{m}$ for the optimal grating parameters for the L-band ($2.9 - 4.1\,\mu\text{m}$): $\Lambda = 1.21\,\mu\text{m}$, $F = 0.5373$, $h = 5.5343\,\mu\text{m}$, $\alpha = 2.45°$.

compute the null depth of the full AGPM by weighting the null depth of both regions by the incident flux on them. Using the AGPM with different f-numbers changes the size of the Airy disk (a smaller f-number resulting in a smaller Airy pattern), and therefore the influence of the central leakage region, which also changes the overall null depth.

The relative importance of the central leakage term may vary for different grating parameters of the AGPM. It is important to understand how these parameters influence the amount of central leakage, and therefore the overall null depth, in order to understand how deviations from optimal design parameters due to manufacturing uncertainties affect the AGPM performance. We performed several simulations with non-optimal grating parameters. These simulations show

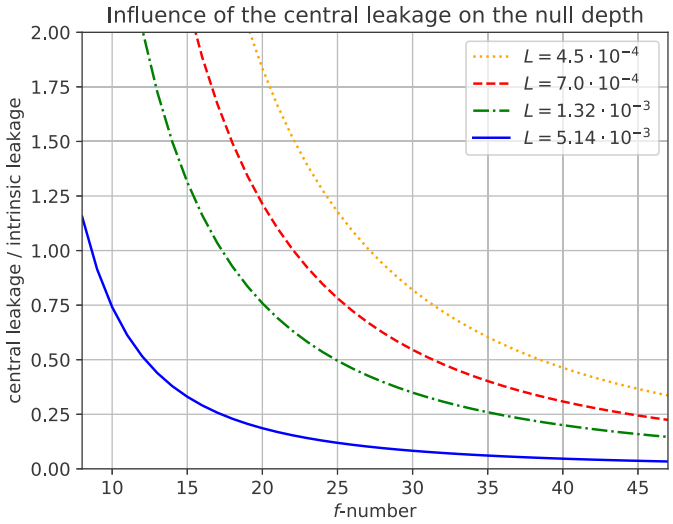

Fig. 6. Relative contribution of the central leakage term to the null depth, displayed as the ratio of the central leakage term to the intrinsic leakage as a function of the f-number. The curves for four different values of the intrinsic leakage L are shown.

Optics EXPRESS

that the relative contribution of the central leakage depends on the intrinsic leakage of the parallel grating. This is due to the fact that the central leakage changes more slowly than the intrinsic leakage when changing the grating parameters. Figure 6 shows the influence of a higher intrinsic leakage of the parallel grating on the contribution of the central leakage to the null depth. The importance of the central leakage term increases when the intrinsic leakage of the straight grating geometry decreases, and when the f-number on the AGPM decreases. This means that, for high-performance AGPMs with optimal manufactured grating parameters, the central leakage term will be more important than for AGPMs with lower intrinsic performance. The central leakage term will also be more important when using the AGPM at small f-numbers.

4. Experimental validation

From the results of the previous section we can calculate the influence of the central leakage on the null depth of the full AGPM. This result can be compared to the null depth measurements on our infrared coronagraphic test bench, referred to as VODCA [24]. VODCA uses a setup as shown in Fig. 2 with a Lyot stop undersized by 80%. Note however that the interpretation of possible discrepancies between predictions and measurements is not straightforward since the manufacturing uncertainty on the grating parameters can have an important influence on the null depth. That means that a poor performance of an AGPM can be both due to manufacturing errors, or to the central leakage term. A possible way to circumvent this problem is to operate the bench with varying f-number. Figure 7 shows the simulated null depth for the most probable grating parameters of AGPM-L5 [11], currently available in our lab, for different f-numbers. The grating parameters are difficult to infer from non-destructive methods. This uncertainty on the grating parameters translates into an error on the simulated null depth of up to around 20%, which is not shown in Fig. 7 for the sake of clarity. For large f-numbers, the region of central leakage is small compared to the size of the illuminating Airy pattern, and the central leakage has little influence on the null depth. For smaller f-numbers, the size of the Airy pattern decreases, and the central leakage becomes more important, resulting in a significant increase of the null depth. For AGPM-L5, with a central pillar of diameter $1.62F\Lambda$, the central leakage would contribute 17 % to the null depth of the AGPM at f/47, the default f-number of VODCA. At f/17, which corresponds to the case of the future METIS instrument at the Extremely Large Telescope [1], the central leakage would contribute a more significant 60 % to the null depth. For smaller f-numbers, the central leakage term would become even more important.

We tested these predictions on VODCA using two different pupil diameters (12.9 mm and 21.9 mm), which correspond to effective f-numbers of f/47 and f/28. The lower limit of the f-number is defined by the maximal diameter of our beam. The upper limit is chosen small enough to show a significant change in performance while keeping a reasonable signal-to-noise ratio on the detector. We measured the null depth for AGPM-L5 with VODCA as described in [24], and show the results in Table 1. The resulting performance ratio is illustrated in Fig. 8. The error bars on the wavelength (horizontal) represent the spectral bandwidth of the filters used on VODCA, while the error bars on the performance increase (vertical) represent the uncertainty typically observed when measuring the null depths on VODCA. The measurement error is much smaller than the measured difference, except for filter L1 where it is in the same order. In any case we are comfortably above the null depth floor introduced by wavefront errors on VODCA, which is below 10^{-4}, as demonstrated in [24]. Our results confirm the predicted influence of the central leakage term on the null depth, which is more pronounced for small f-numbers. It is therefore crucial to minimize the central leakage contribution by optimizing the AGPM design at the center.

Optics EXPRESS

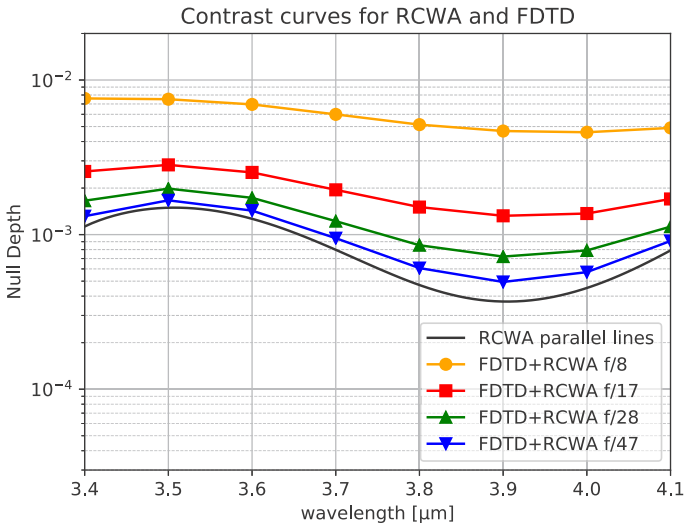

Fig. 7. Estimated spectral null depth for AGPM-L5 (grating parameters: $\Lambda = 1.42\,\mu m$, $F = 0.4320$, $h = 4.6820\,\mu m$, $\alpha = 2.70°$) calculated with RCWA (black) and combining FDTD and RCWA assuming different f-numbers (colored). The low number of simulation points is due to the high computational cost of FDTD.

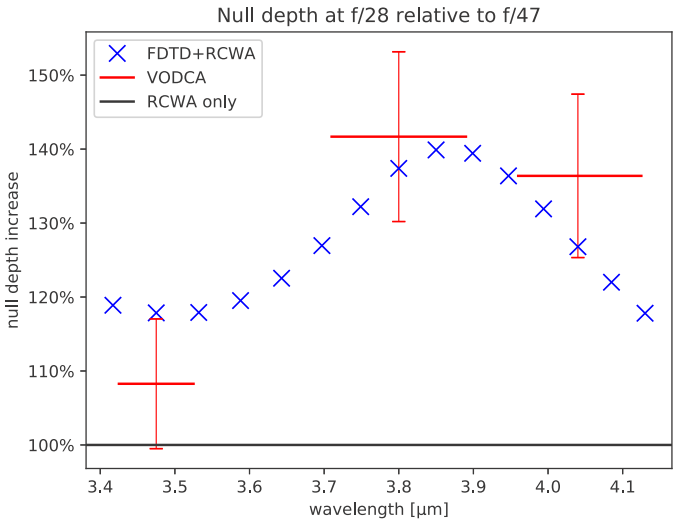

Fig. 8. Ratio of the null depth at f/28 to the null depth at f/47 as measured on the VODCA bench for AGPM-L5 (red bars), compared with FDTD+RCWA simulations (blue crosses) along with RCWA-only simulations (black line). The horizontal width of the red bars corresponds to the spectral bandwidth of the VODCA filters.

Table 1. Null depth measured on VODCA for AGPM-L5 at different *f*-numbers.

	Filter L1 (3425-3525 nm)	Filter L2 (3710-3890 nm)	Filter L3 (3960-4120 nm)
f/28	$(2.62\pm0.15)\times10^{-3}$	$(7.02\pm0.40)\times10^{-4}$	$(1.32\pm0.08)\times10^{-3}$
f/47	$(2.39\pm0.14)\times10^{-3}$	$(4.62\pm0.26)\times10^{-4}$	$(8.94\pm0.51)\times10^{-4}$

Optics EXPRESS

5. Optimized design of the AGPM center

The central part of the AGPM may contribute a considerable amount of leakage to the null depth when operated in configurations with small f-numbers. One possible solution is to adapt the central design to minimize the leakage term arising from the curvature of the grating. For this purpose, we start by exploring several values for the central pillar diameter, and whether a pillar or a hole at the center yields the best performance. A graphical table of our simulation results for a set of central designs and various operating wavelengths is shown in Appendix A, where the size of the pillar or hole is given at the top of the grating. The central leakage of the different designs is summarized in Fig. 9. Simulations for a hole of diameter smaller than 1 µm are not performed because of the finite side wall angle of the grating: when the hole size becomes too small, the side walls merge, which makes the manufacturing process unpredictable. The optimal performance is reached with a central pillar of size 1.0 µm = $1.6F\Lambda$, which is (by pure coincidence) close to the range of pillar sizes that was used for the AGPMs manufactured so far ($1 - 2F\Lambda$).

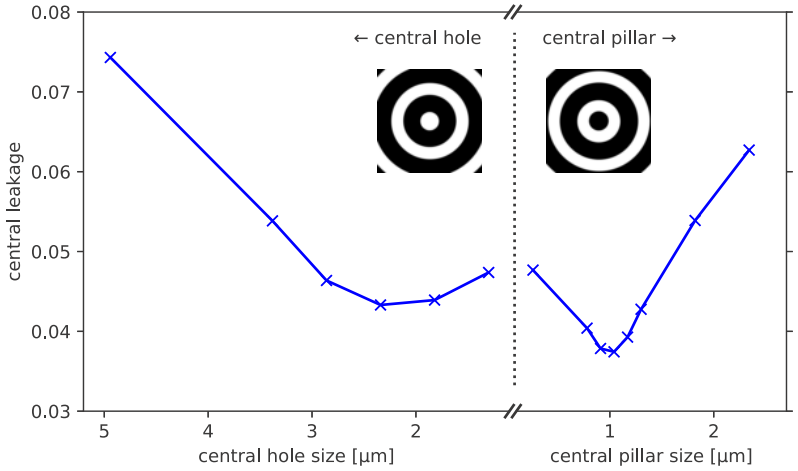

Fig. 9. Simulated central leakage of an optimal AGPM for the L-band (2.9 − 4.1 µm, grating parameters: $\Lambda = 1.21$ µm, $F = 0.5373$, $h = 5.5343$ µm, $\alpha = 2.45°$) for different size of the central pillar or hole. The best performance is reached at a central pillar of diameter 1.0 µm corresponding to $1.6F\Lambda$.

Another way to optimize the central design is to introduce a gradient in the period and filling factor in the central region ($r<r_0$) [13,26], using the following form:

$$\Lambda(r<r_0) = \Lambda_0 + \nabla\Lambda \cdot (r_0 - r)\,,$$
$$F(r<r_0) = F_0 + \nabla F \cdot (r_0 - r)\,,$$

with Λ_0 and F_0 being the optimal grating period and filling factor for a straight grating (denoted Λ and F in the previous sections), r the distance from the AGPM center, $r_0 = 5\Lambda_0$ the radius of the central region, and where $\nabla\Lambda$ and ∇F are the gradient parameters to be optimized. We performed an exploration of the parameter space spanned by the two gradients $\nabla\Lambda$ and ∇F. The results are shown in Fig. 10. For clarity, we show the grating design for selected points of the parameter space as insets. Here, we limit our simulations to the relevant region of the parameter space, where both the subwavelength condition and manufacturing limits (minimal feature size) are fulfilled. Also, we are constraint by the finite side wall angle leading to a region of the parameter space which is challenging to manufacture (green region). The central leakage at the

Optics EXPRESS

optimal parameters $\nabla F = 0.0033$ and $\nabla\Lambda = -0.0708$ (green cross) is reduced by 8 % compared to the design with $\nabla F = 0$ and $\nabla\Lambda = 0$ used so far (red cross). This would lead to a limited improvement in the total null depth of <1 % on VODCA and <5 % for METIS, at the expense of a more challenging manufacturing process.

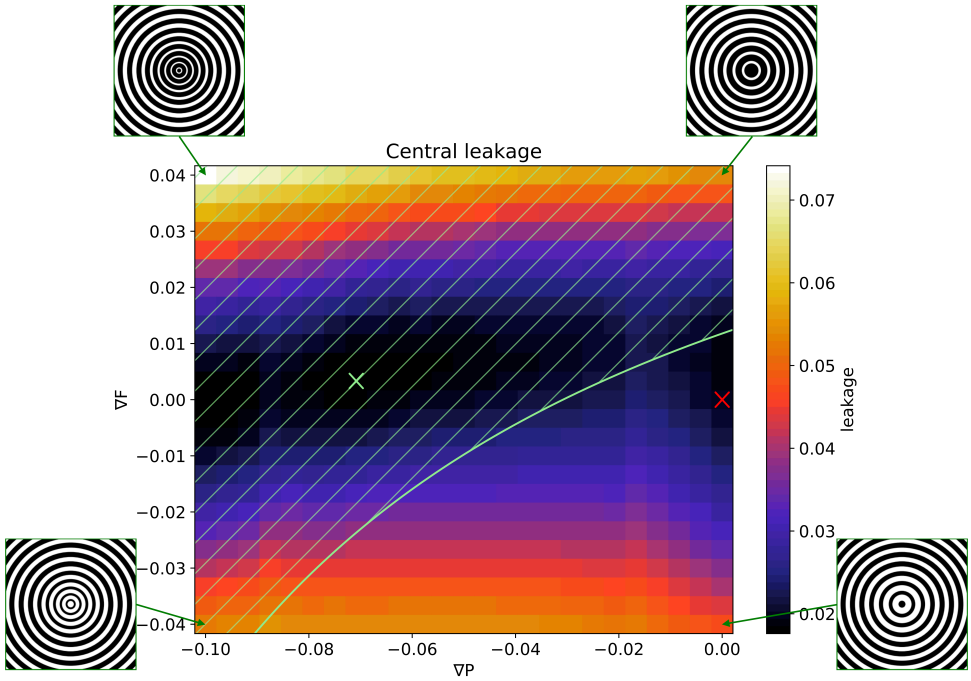

Fig. 10. Leakage map of the parameter space spanned by the gradient of the period $\nabla\Lambda$ and of the filling factor ∇F in the innermost 5Λ. Several insets of the central design are shown for selected points of the parameter space. The optimum is marked with a green cross, the design with constant period and filling factor is marked as red cross. The region above the green line is challenging to manufacture because of the finite side wall angle of the grating. The optimal grating parameters for the L-band (2.9 – 4.1 µm) are used: $\Lambda = 1.21$ µm, $F = 0.5373$, $h = 5.5343$ µm, $\alpha = 2.45°$.

6. Conclusion

Throughout this paper we have shown that the FDTD code MEEP is an appropriate tool for simulating the center of the AGPM, which was not possible so far with RCWA. Using MEEP, we determined the size of the central leakage region where the validity conditions of RCWA are not granted anymore due to the curved nature of the grating. For a reasonable size of the central pillar, this limit is found to be at 5 Λ from the center. This result means that we can rely on RCWA beyond this limit and that we only need to simulate a small part of the full AGPM with computationally costly FDTD. Using these results, we estimated the central leakage contribution to the null depth of the full AGPM for different f-number configurations. We conclude that the AGPM performs best when operated at high f-numbers, because the central leakage term only covers a small part of the Airy disk on the AGPM. We confirmed these results on our coronagraphic test bench VODCA at different f-numbers. To reduce the strength of the central leakage, we finally investigated several designs of the AGPM center including a pillar or hole of different size at the center. Our simulations show that using a pillar of size $1.6F\Lambda$ minimizes the

Optics EXPRESS

central leakage. We also suggest that a progressive change in period and filling factor could also improve the AGPM performance by few percent.

The simulation framework presented in this paper has proven to be suited to describe a finite patch of the AGPM center. It can be extended to investigate arbitrary designs of vortex phase masks, including segmented designs and full-metasurface patterns, which will be needed to design and simulate vortex phase masks of higher topological charge.

A. Appendix: leakage maps for different central designs

The design of the AGPM center influences the size of the central leakage region. In Figs. 11 and 12, we show the simulation results for a series of different values for the central pillar (or hole) diameter. The main leakage contribution is localized within the first 5 Λ for designs with a central pillar. The leakage distribution is broader for designs with a central hole. Note that the design shown is a cut at half height of the grating, as it is more representative of the material distribution, but the hole or pillar diameter is the nominal value at the top of the grating.

Optics EXPRESS

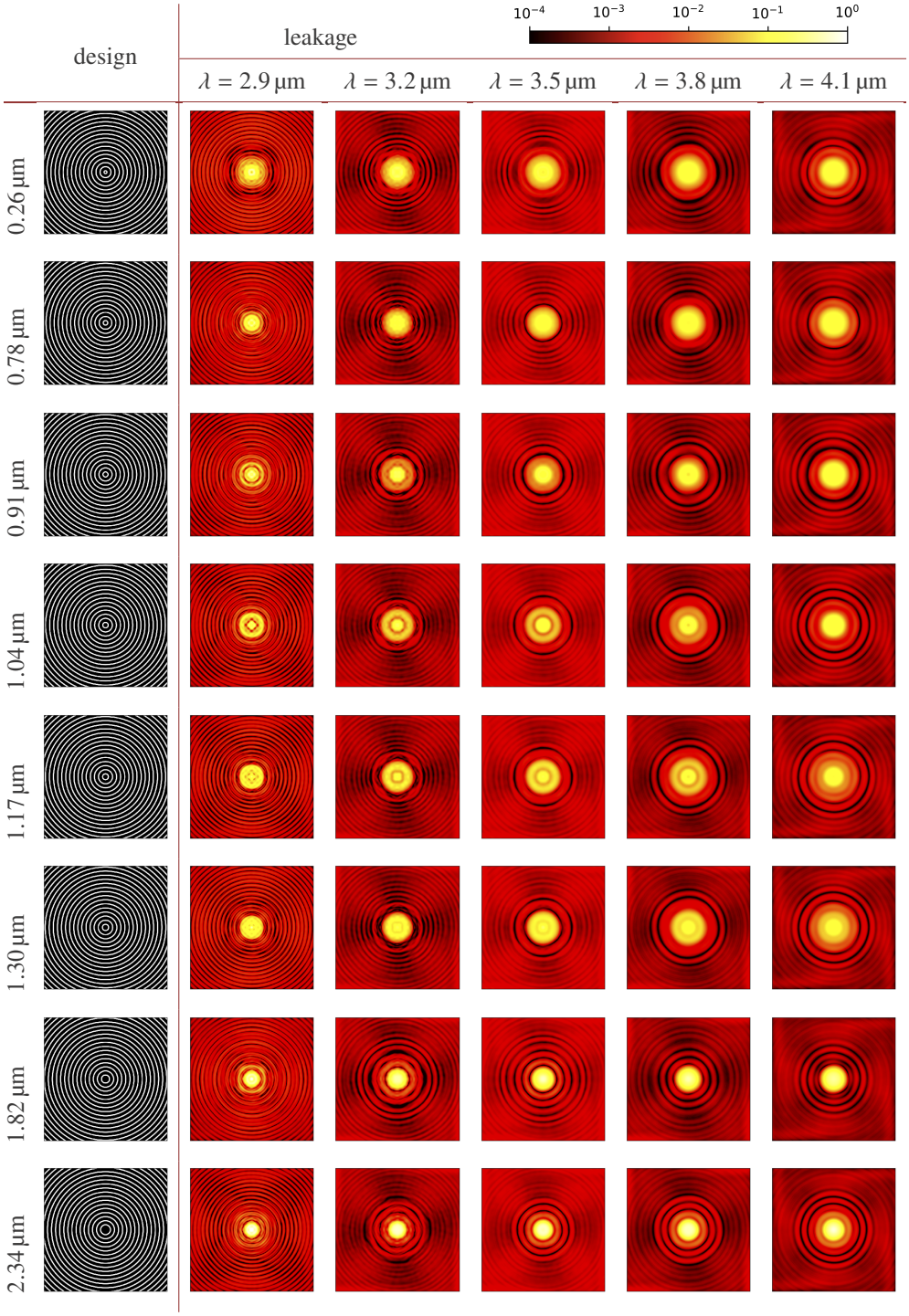

Fig. 11. Leakage for several designs with different central pillar size. From left to right: nominal diameter of the central pillar, design, and leakage maps for 5 wavelengths in the *L*-band (2.9 – 4.1 µm).

Optics EXPRESS

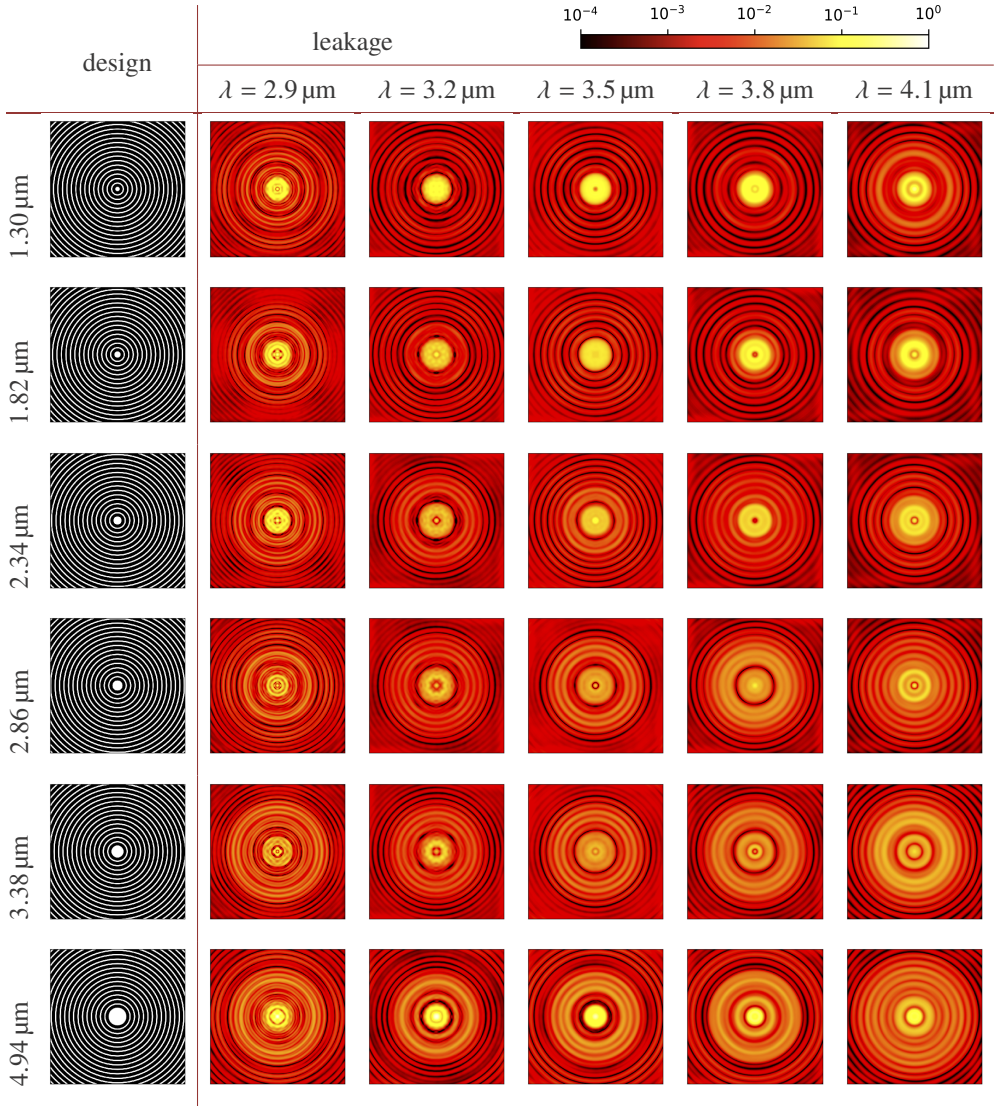

Fig. 12. Leakage for several designs with different central hole size. From left to right: nominal diameter of the central hole, design, and leakage maps for 5 wavelengths in the *L*-band (2.9 – 4.1 µm).

Funding. European Research Council (819155).

Acknowledgments. Some of the required computational resources were provided by the Consortium des Équipements de Calcul Intensif (CÉCI), funded by the Fonds de la Recherche Scientifique de Belgique (F.R.S.-FNRS) under Grant No 2.5020.11, and by the Walloon Region.

Disclosures. The authors declare no conflicts of interest.

Data availability. The simulation tools leading to the results presented in this paper are publicly available in Ref. [27].

Optics EXPRESS

References

1. B. Brandl, F. Bettonvil, R. van Boekel, A. Glauser, S. Quanz, O. Absil, A. Amorim, M. Feldt, A. Glasse, M. Güdel, P. Ho, L. Labadie, M. Meyer, E. Pantin, H. van Winckel, and METIS Consortium, "METIS: The Mid-infrared ELT Imager and Spectrograph," The Messenger **182**, 22–26 (2021).
2. G. Ruane, E. Serabyn, C. Mejia Prada, W. Baxter, E. Bendek, D. Mawet, and A. J. E. Riggs, "Experimental analysis of the achromatic performance of a vector vortex coronagraph," Proc. SPIE **11443**, 114432O (2020).
3. D. Mawet, P. Riaud, O. Absil, and J. Surdej, "Annular Groove Phase Mask Coronagraph," Astrophys. J. **633**(2), 1191–1200 (2005).
4. C. Delacroix, O. Absil, D. Mawet, C. Hanot, M. Karlsson, P. Forsberg, E. Pantin, J. Surdej, and S. Habraken, "A diamond AGPM coronagraph for VISIR," Proc. SPIE **8446**, 84468K (2012).
5. D. Mawet, O. Absil, C. Delacroix, J. H. Girard, J. Milli, J. O'Neal, P. Baudoz, A. Boccaletti, P. Bourget, V. Christiaens, P. Forsberg, F. Gonte, S. Habraken, C. Hanot, M. Karlsson, M. Kasper, J. L. Lizon, K. Muzic, R. Olivier, E. Pe na, N. Slusarenko, L. E. Tacconi-Garman, and J. Surdej, "L'-band AGPM vector vortex coronagraph's first light on VLT/NACO. Discovery of a late-type companion at two beamwidths from an F0V star," Astron. & Astrophys. **552**, L13 (2013).
6. D. Defrère, O. Absil, P. Hinz, J. Kuhn, D. Mawet, B. Mennesson, A. Skemer, K. Wallace, V. Bailey, E. Downey, C. Delacroix, O. Durney, P. Forsberg, C. Gomez Gonzales, S. Habraken, W. F. Hoffmann, M. Karlsson, M. Kenworthy, J. Leisenring, M. Montoya, L. Pueyo, M. Skrutskie, and J. Surdej, "L'-band AGPM vector vortex coronagraph's first light on LBTI/LMIRCam," Proc. SPIE **9148**, 91483X (2014).
7. E. Serabyn, E. Huby, K. Matthews, D. Mawet, O. Absil, B. Femenia, P. Wizinowich, M. Karlsson, M. Bottom, R. Campbell, B. Carlomagno, D. Defrère, C. Delacroix, P. Forsberg, C. Gomez Gonzalez, S. Habraken, A. Jolivet, K. Liewer, S. Lilley, P. Piron, M. Reggiani, J. Surdej, H. Tran, E. Vargas Catalán, and O. Wertz, "The W. M. Keck Observatory Infrared Vortex Coronagraph and a First Image of HIP 79124 B," Astron. J. **153**(1), 43 (2017).
8. G. Biener, A. Niv, V. Kleiner, and E. Hasman, "Formation of helical beams by use of Pancharatnam–Berry phase optical elements," Opt. Lett. **27**(21), 1875–1877 (2002).
9. D. Rouan, P. Riaud, A. Boccaletti, Y. Clénet, and A. Labeyrie, "The Four-Quadrant Phase-Mask Coronagraph. I. Principle," Publ. Astron. Soc. Pac. **112**(777), 1479–1486 (2000).
10. D. Mawet, P. Riaud, J. Surdej, and J. Baudrand, "Subwavelength surface-relief gratings for stellar coronagraphy," Appl. Opt. **44**(34), 7313–7321 (2005).
11. E. Vargas Catalán, E. Huby, P. Forsberg, A. Jolivet, P. Baudoz, B. Carlomagno, C. Delacroix, S. Habraken, D. Mawet, J. Surdej, O. Absil, and M. Karlsson, "Optimizing the subwavelength grating of L-band annular groove phase masks for high coronagraphic performance," Astron. & Astrophys. **595**, A127 (2016).
12. D. Mawet, E. Serabyn, K. Liewer, C. Hanot, S. McEldowney, D. Shemo, and N. O'Brien, "Optical Vectorial Vortex Coronagraphs using Liquid Crystal Polymers: theory, manufacturing and laboratory demonstration," Opt. Express **17**(3), 1902–1918 (2009).
13. N. Yu and F. Capasso, "Flat optics with designer metasurfaces," Nat. Mater. **13**(2), 139–150 (2014).
14. S. Kruk, F. Ferreira, N. Mac Suibhne, C. Tsekrekos, I. Kravchenko, A. Ellis, D. Neshev, S. Turitsyn, and Y. Kivshar, "Transparent dielectric metasurfaces for spatial mode multiplexing," Laser Photonics Rev. **12**(8), 1800031 (2018).
15. M. Khorasaninejad, W. T. Chen, R. C. Devlin, J. Oh, A. Y. Zhu, and F. Capasso, "Metalenses at visible wavelengths: Diffraction-limited focusing and subwavelength resolution imaging," Science **352**(6290), 1190–1194 (2016).
16. X. Liu, J. Deng, K. F. Li, M. Jin, Y. Tang, X. Zhang, X. Cheng, H. Wang, W. Liu, and G. Li, "Optical telescope with Cassegrain metasurfaces," Nanophotonics **9**(10), 3263–3269 (2020).
17. R. C. Devlin, A. Ambrosio, D. Wintz, S. L. Oscurato, A. Y. Zhu, M. Khorasaninejad, J. Oh, P. Maddalena, and F. Capasso, "Spin-to-orbital angular momentum conversion in dielectric metasurfaces," Opt. Express **25**(1), 377–393 (2017).
18. K. E. Chong, I. Staude, A. James, J. Dominguez, S. Liu, S. Campione, G. S. Subramania, T. S. Luk, M. Decker, D. N. Neshev, I. Brener, and Y. S. Kivshar, "Polarization-Independent Silicon Metadevices for Efficient Optical Wavefront Control," Nano Lett. **15**(8), 5369–5374 (2015).
19. M. I. Shalaev, J. Sun, A. Tsukernik, A. Pandey, K. Nikolskiy, and N. M. Litchinitser, "High-Efficiency All-Dielectric Metasurfaces for Ultracompact Beam Manipulation in Transmission Mode," Nano Lett. **15**(9), 6261–6266 (2015).
20. M. G. Moharam and T. K. Gaylord, "Rigorous coupled-wave analysis of planar-grating diffraction," J. Opt. Soc. Am. **71**(7), 811–818 (1981).
21. C. Delacroix, P. Forsberg, M. Karlsson, D. Mawet, O. Absil, C. Hanot, J. Surdej, and S. Habraken, "Design, manufacturing, and performance analysis of mid-infrared achromatic half-wave plates with diamond subwavelength gratings," Appl. Opt. **51**(24), 5897–5902 (2012).
22. L. König, O. Absil, C. Delacroix, M. Lobet, M. Karlsson, E. Vargas Catalán, G. Orban de Xivry, J. Loicq, and S. Habraken, "Vortex Phase Masks of Topological Charge 4 and higher with Diamond Subwavelength Gratings," Proc. SPIE **11451**, 1145144 (2020).
23. A. F. Oskooi, D. Roundy, M. Ibanescu, P. Bermel, J. D. Joannopoulos, and S. G. Johnson, "MEEP: A flexible free-software package for electromagnetic simulations by the FDTD method," Comput. Phys. Commun. **181**(3), 687–702 (2010).

Optics EXPRESS

24. A. Jolivet, G. Orban de Xivry, E. Huby, P. Piron, E. Vargas Catalán, S. Habraken, J. Surdej, M. Karlsson, and O. Absil, "L- and M-band annular groove phase mask in lab performance assessment on the vortex optical demonstrator for coronagraphic applications," J. Astron. Telesc. Instrum. Syst. **5**(02), 1 (2019).
25. A. F. Oskooi and S. G. Johnson, "Distinguishing correct from incorrect PML proposals and a corrected unsplit PML for anisotropic, dispersive media," J. Comput. Phys. **230**(7), 2369–2377 (2011).
26. N. Yu, P. Genevet, M. A. Kats, F. Aieta, J.-P. Tetienne, F. Capasso, and Z. Gaburro, "Light Propagation with Phase Discontinuities: Generalized Laws of Reflection and Refraction," Science **334**(6054), 333–337 (2011).
27. L. König, "Supporting material for König et al. (2022), Optimal Design of the Annular Groove Phase Mask Central Region," https://github.com/LorenzoKonig/Konig22-AGPM-center (2022). Accessed: 13 June 2022.